4.1 Introduction

Topological Insulators (TIs) contain interesting gapless metallic surface states, which can be distinguished from their insulating bulk. The topological surface states (TSS) are invariant topologically with Time Reversal Symmetry (TRS) [4], [118], [141] and are also protected from electronic backscattering due to the spin-momentum helical locking, thus enhancing the expectation to show high quantum coherency in charge and spin transport [142]. Inducing magnetic and non-magnetic transition metal ions into the basic TIs like Bi_2Te_3, Sb_2Te_3 and Bi_2Se_3, the spin-induced properties can be enhanced to apply TIs as high storage memory devices, faster quantum computational devices and spintronics devices. However, strong magnetic ions like Fe, Co, and Mn introduce spontaneous magnetic moments inside the non-magnetic TI structures creating local magnetic domains [40], [143]–[147]. Ideally, antiferromagnetic (AFM) ordering is introduced in TIs at very low temperatures injecting transition metals and rare earth materials with half-filled conduction bands. But, recently iron (3-D transition metal) doped $Bi_2(SeS)_3$ exhibits giant ferromagnetic (FM) ordering at a wide range of temperatures below 550 K [42]. Such room temperature ferromagnetic ordering in presence of the magnetic impurity potentially violates the TRS opening a finite gap at the Dirac point. Such phenomena modify the topological surface state virtually at lower dimensions inducing the strain modulated consequences to use such quantum materials potentially at a large scale [148]. Also, at the lower dimension, there is a certain probability to exhibit the signature of weak anti-localization (WAL) in accordance with the fact that such a nontrivial confined system might have a robust topological surface state, regardless of any nonmagnetic impurities [149], [150]. Magnetic ion-based thin films of TIs are possible to use practically at various faster quantum and magnetic logic devices. As an example, in Bi_2Te_3 thin film on top of the iron-based superconductor $FeTe_{0.55}Se_{0.45}$, the superconducting proximity effect was induced and

probed by STM/STS measurements indicating a twofold symmetry of the order parameter and an elongated vortex structure [151]. Similarly, we considered another iron chalcogenide type material FeSe exhibiting a tetragonal phase or a hexagonal phase structure, depending on the structural transformation by modifying the atomic concentration of Fe and Se in FeSe. FeSe shows superconductivity at low temperatures (below 9 K) and thus can be applied potentially like spin injection materials in spintronics [152]. Also, tetragonal FeSe exhibits ferromagnetism beyond room temperature. Therefore, we introduced such a dramatic transition ion-based material as the magnetic impurity in the Bi_2Se_3 single crystalline TI to modify its structural, electronic, and physical properties. Also, we intended to prepare FM/TI/FM heterostructures to compare the magnetic proximity effects with the bulk topological insulators using such iron-based high-temperature ferromagnets into Bi_2Se_3 type conventional TIs. This might impede a detailed momentum-resolved characterization of the electronic structure disclosing gaps at the Dirac cone for both the topological surface states and bulk states. Such heterostructural systems are therefore promising for quantum information devices, spintronics applications, or faster quantum computation.

We prepared all the bulk single crystals $(Bi_2Se_3)_{1-x}(FeSe)_x$ using modified Bridgeman technique (Discussed in section 2.2.1) and polycrystals of FeSe using solid state synthesis method as described in section 2.2.2. Then heterostructure of FeSe/Bi_2Se_3/FeSe was prepared using PLD technique after following the calibration procedure discussed in section 2.2.3. Then we carried out all the structural and morphological analysis to check the purity of as prepared systems followed by electronic, physical and magnetic measurements to compare the topological properties of the prepared bulk and heterostructure systems.

4.2 Results and Discussion

4.2.1 Structural and Morphological Analysis

To identify the crystal structure and respective lattice parameters of the prepared single crystals and heterostructure, we carried out powder XRD measurements. The perfect single-crystalline nature of the prepared $(Bi_2Se_3)_{1-x}(FeSe)_x$ (x = 0.05, 0.1) (we have denoted the prepared single crystals as FSBS5 and FSBS10 simultaneously) crystals were exhibited in Figure 4.1 (a), while XRD was done on the mechanically cleaved easy plane of the prepared crystals. The easy plane is basically the plane (ab-plane) perpendicular to the crystal growth (c-axis) as the prepared crystals exhibit a layered structure. The layered structures were evidenced by the micro-morphological analysis using FESEM images as shown in the insets of Figure 4.1 (a). The average layer thickness was calculated as 0.88 µm for FSBS5 and 0.67 µm for FSBS10. Also, the elemental compositions were examined for all the samples using energy dispersive X-ray (EDX) and tabulated as shown in the inset of Figure 4.1 (a). Further, we investigated the Rietveld refinement of the XRD patterns of FSBS5 and FSBS10 crystals using the Fullprof software as shown in Figure 4.1 (b). Analyzing the refinement results, we confirmed the single-phase formation of the prepared single crystals as the rhombohedral structure of space group $R\bar{3}m$ [40], [42]. The variation of lattice parameters with the doping concentration is tabulated in Table 4.1 which follows Vegard's law [153], [154]. Further, the crystalline nature of the prepared FS/BS/FS heterostructure was confirmed by performing the Grazing Angle X-ray Diffraction technique (GAXRD) at an angle 0.65˚ and compared with the XRD patterns of the target materials (Figure 4.1 (c)). In order to recognize the surface profile and measure the grain size of the as-prepared heterostructure, FESEM images were studied over the surfaces (Figure 4.1 (d)). The well-distributed hexagonal grains support that the growth of the films is along the c-axis and the average grain size was calculated as 283 nm for FS/BS/FS over
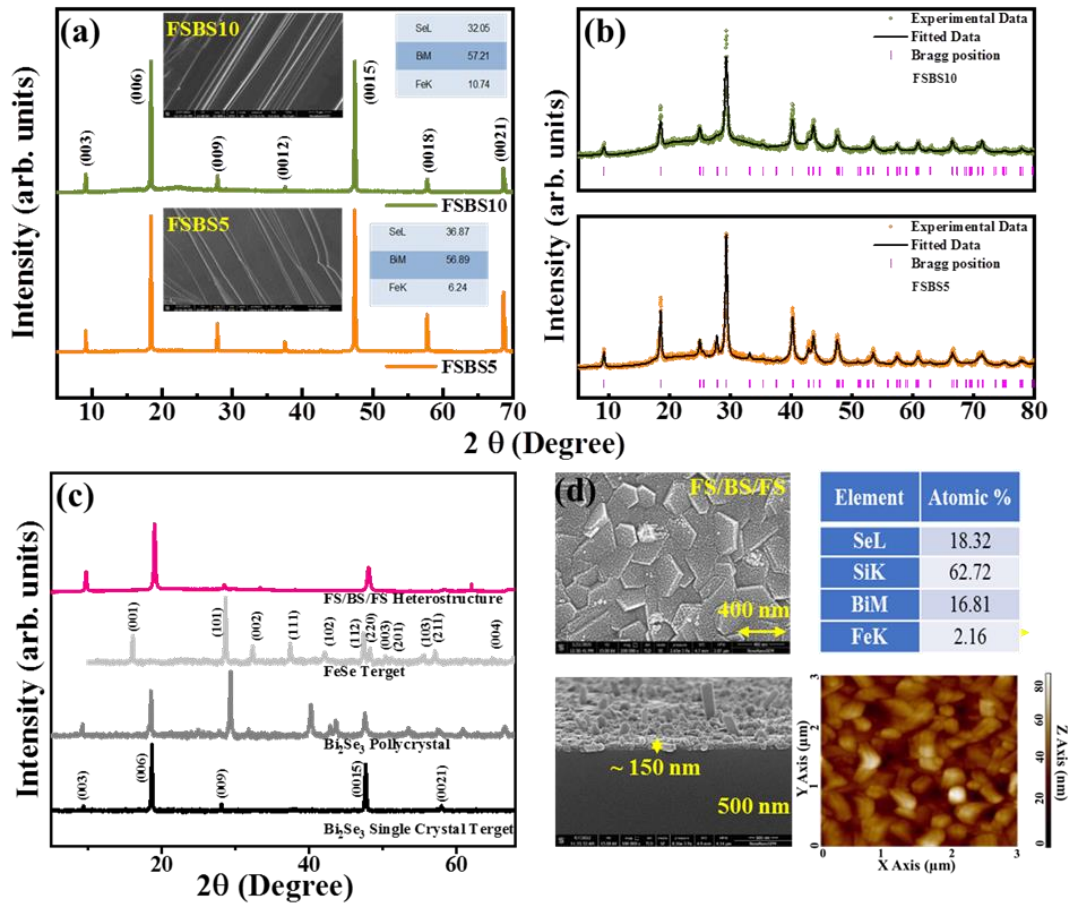
Figure 4.1: (a) Single crystal XRD pattern of the FSBS5 and FSBS10. The cross-sectional FESEM images along with EDX profiles are shown in the insets for both the crystals. (b) The powder XRD of FSBS5 and FSBS10 refined by Rietveld pattern. (c) XRD analysis of the prepared heterostructures compared with the used target materials. (d) Surface and cross-sectional FESEM images of as-prepared heterostructure are exhibited in the left column. The atomic concentration from EDX analysis is shown in the top right table. In the bottom right, the AFM height profile is displayed.

Table 4.1 Structural parameters evaluated from Rietveld refinement of the powder XRD patterns of the single crystals.

Crystal	a (Å)	b (Å)	c (Å)	α	B	γ
$(Bi_2Se_3)_{0.85}(FeSe)_{0.05}$	4.143197	4.143197	28.677496	90°	90°	120°
$(Bi_2Se_3)_{0.9}(FeSe)_{0.1}$	4.144118	4.144118	28.689827	90°	90°	120°

the surface. Further, the thickness of the heterostructure was determined by performing the cross-sectional FESEM observation as shown in the bottom left corner of Figure 4.1 (d). The average thickness of the prepared FS/BS/FS heterostructure was evaluated as around ~ 150 nm. Also, the atomic concentration was evaluated using EDX

over the film and tabulated in the top right corner of Figure 4.1 (d). Analyzing the atomic concentrations of all the elements, it can be anticipated that the FeSe layer is much thinner than the Bi_2Se_3 layer which was further confirmed by XPS depth profile analysis. Furthermore, the average surface roughness was evaluated as 9.005 nm using AFM analysis using intermittent contact mode and exhibited in the bottom left corner of Figure 4.1 (d) which displays the inter-connected truncated wedge-shaped and hexagonally moulded granular surface of the film. Also, the root-mean-square (rms) surface roughness was obtained to be 10.404 nm for a 3 µm × 3 µm scanned area. Moreover, the layer-by-layer atomic profile matrix along with thickness confirmation of the heterostructure is discussed in the next section, by analyzing the XPS spectra.

4.2.2 Electronic Property

To acquire knowledge about the electronic structures of the single crystalline bulk dominating systems and to compare the same with the prepared heterostructure we have performed an XPS survey scan and elemental scan of all the above-described systems. Hence, we compared all the spectral positions of the present elements and their significant doublet separations of the measured XPS spectra with the National Institute of Standards and Technology (NIST) XPS database. For both FSBS5, and FSBS10 crystals and FS/BS/FS heterostructure the XPS survey scan confirms that the elements Fe, Se, and Bi are present in the systems as shown in Figure 4.2 (a). However, no impurity elements were found other than C (1s) which usually get absorbed at the surface under air exposure, for all the systems [155], [156]. The core-level XPS spectra of all three elements in terms of binding energy (BE) are shown in Figure 4.2 (b-d) for FSBS5 and Figure 4.2 (e-g) for FSBS10. Both the single crystals exhibited the spin-orbit split peaks Bi-4f$_{7/2}$ and Bi-4f$_{5/2}$ around 158 eV and 163.3 eV containing doublet separation of ~ 5.3 eV as shown in Figure 4.2 (b, e). Further, two more deconvoluted peaks are positioned around 165.1 eV and 159

eV, which might be corresponding to the Bi 5+ oxidation states of Bi [157], [158]. This Bi 5+ peak might carry the trace of the Bi-O bonds due to the surface air exposure of the respective crystals. But, the dominating Bi-4f (Bi 3+) peaks are slightly blue-shifted with respect to the elemental Bi peaks and correspond to the Bi-Se bonds of Bi_2Se_3 [157]. Core-level XPS spectra for Se-$3d_{5/2}$ and Se-$3d_{3/2}$ were deconvoluted using the Lorentzian fitted function and the peak positions were found to be around 53.6 eV and 54.5 eV (with 0.9 eV crystal splitting) for both single crystals exhibited in Figure 4.2 (c, f) which is consistent with the previous results [157], [158] and slightly red-shifted concerning to the Se-Se bonds. Thus, the Bi-4f and Se-3d peaks are shifted slightly in opposite direction confirming the charge transfer mechanism from the Bi to Se site and the formation of Bi-Se bonds. Further, the XPS spectra from 705 eV to 730 eV were deconvoluted into Fe-$2p_{3/2}$ and Fe-$2p_{1/2}$ spectral peaks which are positioned around 711 eV and 723.7 eV, respectively having 12.7 eV difference for both the crystals as shown in Figure 4.2 (d, g) [159], [160]. This electronic state of Fe-2p is corresponding to the Fe-Se bond formation with zero valences in FeSe, where Fe replaces Bi atoms and charge is transferred from Fe to Se in both FSBS5 and FSBS10 single crystals [159]. Further, in order to perform the elemental analysis of the prepared heterostructure, we carried out depth profiling [161], [162] in XPS by argon (Ar^+) etching at the rate of 0.51 nm/second over a 2 mm × 4 mm surface. Depth profiling is considered to be an effective analytical technique to evaluate the chemical compositions and atomic profiles of the located materials throughout the matrix of the film. Thus, to identify each layer and interface of the heterostructure we conducted one XPS scan at a particular time spacing of 60 seconds over a particular area (2 mm × 4 mm). Hence, the film surface was engraved by ~30 nm per 60 seconds and scanned repeatedly until it reaches the substrate. Figure 4.3 (a) represents the normalized atomic profile concerning the etched depth (nm) for all the elements present in the FS/BS/FS heterostructure. The first scan was

performed over the unetched surface at etching time = 0. It is clear from Figure 4.3 (a), that the atomic concentration of Fe is maximum at etching time = 0 and etched depth = 0 nm denoting the FeSe layer at the surface. Then, the profile of Bi and Se is high from 30 to 120 nm representing the Bi_2Se_3 as the mid-layer. At 150 nm etched depth, we found high Fe content again, as the third layer is FeSe. And after that, the Si profile increased to its maximum while the other atomic profiles reduced rapidly declaring the end of the heterostructure to its substrate. From this profile, the thickness of the FS/BS/FS heterostructure is demonstrated as ~150 nm confirming the three layers FeSe - Bi_2Se_3 - FeSe exhibiting approximately 30 nm - 90 nm - 30 nm depth. The elemental XPS spectra for Bi, Se, Fe and Si-substrate corresponding to the FS/BS/FS system are shown correspondingly in Figure 4.3 (b-e) at different etching times during depth profile scanning. At the surface of both the films $Bi-4f_{7/2}$ and $Bi-4f_{5/2}$ peaks are slightly shifted (~1.2 eV) along higher BE with respect to the single crystals. The shifted Bi-4f peaks at 159.2 eV and 164.6 eV are denoting the dominance of the Bi 5+ oxidation state which is mostly corresponding to the Bi-O bonds. Usually, such Bi-O bonds exist over the surface due to surface oxidation under the air exposure of post-deposited thin films. When we sputter the film surface with Ar^+ ions under an ultra-high vacuum condition (10^{-6} mbar), the upper surface is removed and the non-oxide film is exposed to examination. Thus, the 2nd scan was performed at 30 nm etched depth at 60 seconds and now we got the $Bi-4f_{7/2}$ and $Bi-4f_{5/2}$ peaks shifted at a very small value as 0.6 eV towards the lower BE side respective to the bulk systems. The positions of the peaks confirm that the Bi atoms are making only Bi-Se bonds with Bi 3+ valency inside the film. And such red-shift arises due to the charging of the surface with Ar^+ ion sputtering which eventually enhances the electron density lowering the BE [162], [163]. The argon etching procedure is continued till the exposure of the substrate. As a result, the Bi-4f peaks continue to shift towards lower BE with very
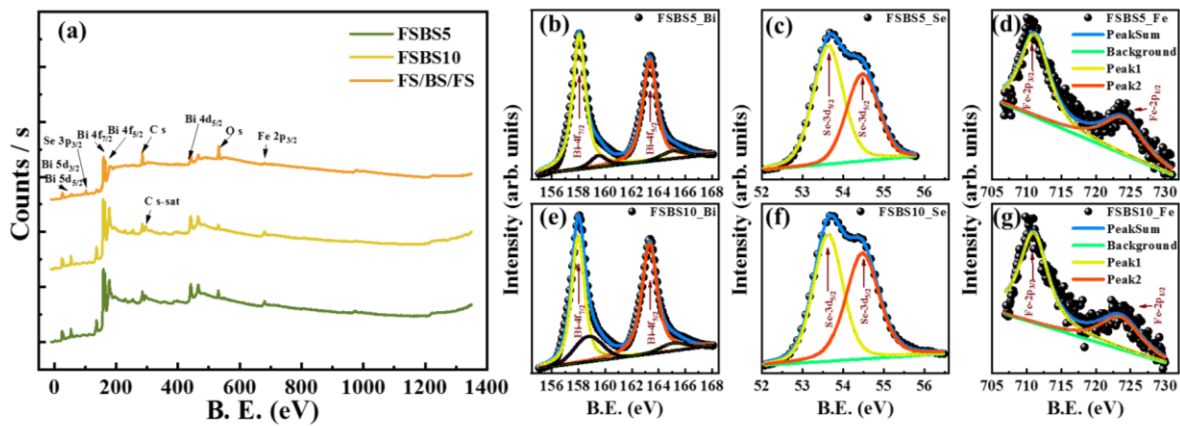
Figure 4.2: (a) XPS survey scan over the FSBS5, FSBS10 and FS/BS/FS systems. (b-d) represents the elemental XPS spectra of the Bi-4f, Se-3d and Fe-2p for FSBS5 single crystal and (e-g) represents the elemental XPS spectra of the Bi-4f, Se-3d and Fe-2p for FSBS10 single crystal.
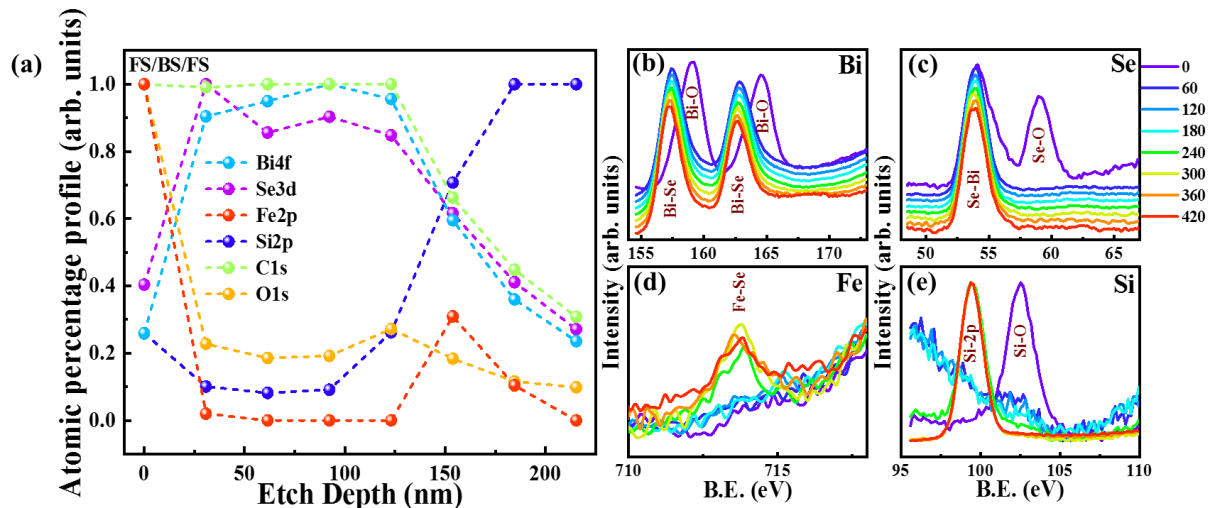
Figure 4.3: (a) XPS atomic percentage profile concerning the etch depth of the FS/BS/FS heterostructure. (b-e) represents the XPS depth profile spectra at different etching times for Bi-4f, Se-3d, Fe-2p and Si-2p elements in FS/BS/FS heterostructure, respectively.

low value as the 6th scan after 300 seconds and 150 nm etched depth displays only 0.3 eV shifting of the BE from the 2nd scan for FS/BS/FS heterostructure (Figure 4.3 (b)). For Se, we scanned electronic states from 50 eV to 65 eV BE for the heterostructure as shown in Figure 4.3 (c). At the surface before etching starts the Se-3d positions were nearly similar to the single crystals with a slight left-shift of 0.4 eV confirming the Bi-Se bond and another peak exists at 59.2 eV which signifies the Se-O bonds at the surface due to the surface oxidation. This Se oxide peak confirms that the oxygen absorption was happened only on

the topmost layer of the prepared thin film [164]. After argon etching for 60 seconds, the peak at 59.2 eV vanishes confirming that the Se-O bond does not exist inside the film. Continuing the etching procedure, the Se-3d peaks were observed to be shifted towards lower BE at very small values till the revelation of the substrate for the heterostructure which is due to the charging effect. But in the film, the Fe-2p peaks are very weak as a result of the low atomic concentration of Fe atoms. The only visible peak in FS/BS/FS, Fe-2p$_{3/2}$ at 713 eV is around 2 eV blue shifted from the single crystals (Figure 4.3 (d)) and sited only after 240 seconds etching at 120 nm depth. This shifting arises might be due to the charge transfer of Fe to Se and lowering of electron density in Fe site. We also scanned Si-2p BE, which shows maxima at 103 eV at the surface. This spectrum is corresponding to the Si-O bond which appears due to the air exposure. After the surface scan the Si substrate was exposed showing Si-2p peak around 99 eV [165] after etching 300 seconds for FS/BS/FS (Figure 4.3 (e)) which supports the thickness profile of the heterostructure. Thus, from the XPS depth profile we analyzed and compared the in-depth electronic structure of all the elements present in both the bulk and low dimensional system. Henceforth to draw a distinct changeover in the intrinsic properties of the as prepared quantum materials transiting from 3-D to 2-D system under 1-D confinement we have investigated possible magnetic and physical phenomena of the aforesaid systems accordingly, which are described in the next section. In this context it is noteworthy to mention that, the thickness of the FS/BS/FS heterostructure which is around 150 nm suggests that material is in the range of thin film (less than 200 nm). Thus, we have considered this heterostructure as the 2-D confined system and carried out all the magnetic and transport measurements over it to compare it with the 3-D single crystals.

4.2.3 Magnetic Property

Further, we would like to mention that many physical properties depend on the magnetic state of the materials. So, we have measured the magnetization of our samples under investigation elaborately. The magnetization (M) vs. temperature (T) data for the zero-field-cooled (ZFC) and field-cooled (FC) FSBS5 and FSBS10 systems at 1000 Oe are exhibited in Figure 4.4 (a) and Figure 4.4 (b), respectively. The corresponding magnetization curves with varying magnetic fields showing mixed ferro and anti-ferromagnetic ordering are demonstrated in Figure 4.4 (c, d) at different temperatures from 3 K to 300 K. At 3 K, the ferromagnetic ordering is dominating below ± 1 T and gradually decreases with raising the temperature. But this is clear from the *M-T* curves (Figure 4.4 (a, b)) that the magnetic ordering is present beyond room temperature for both the single crystals. Such room temperature ferromagnetic ordering is consistent with our previous publication showing the gap opening in the Dirac point in presence of the transition metal ions in Bi_2Se_3 [42]. Further, to recognize the large bifurcation below 300 K we measured ac susceptibility (χ_{ac}) at different frequencies which shows the clear shifting of the peak (near 30 K) in both real (χ'_{ac}) and imaginary (χ''_{ac}) part along the higher temperature side with raising frequency as shown in Figure 4.4 (e, f), respectively for FSBS5 and FSBS10. Such shifting in χ'_{ac} and χ''_{ac} peaks are consistent with the glassy nature of the spins at low temperature [166], [167]. Figure 4.5 (a) is showing the thermal variation of ZFC magnetization of FS/BS/FS heterostructure at 1000 Oe applied field. From this figure, we have observed that the magnetization (M) is not showing any sudden magnetic transition up to 700 K. We also did not observe any inflection point in the dM/dT curve again showing the absence of any sudden magnetic transition [168], [169]. Further, to predict possible spin ordering we have measured the isothermal magnetization of both systems at different temperatures. We have shown the isothermal magnetization for the 2-D system in Figure

4.5 (b) after subtracting the diamagnetic contribution from the experimental data. From the isothermal magnetization, it has been observed that the system shows dominant antiferromagnetic ordering at low temperatures (5 K). This antiferromagnetic ordering usually has been observed in Bi_2Se_3 TI having different magnetic transition metal elements [170], [171]. Also, from the MFM image raster scanned at the inter-mediated contact mode
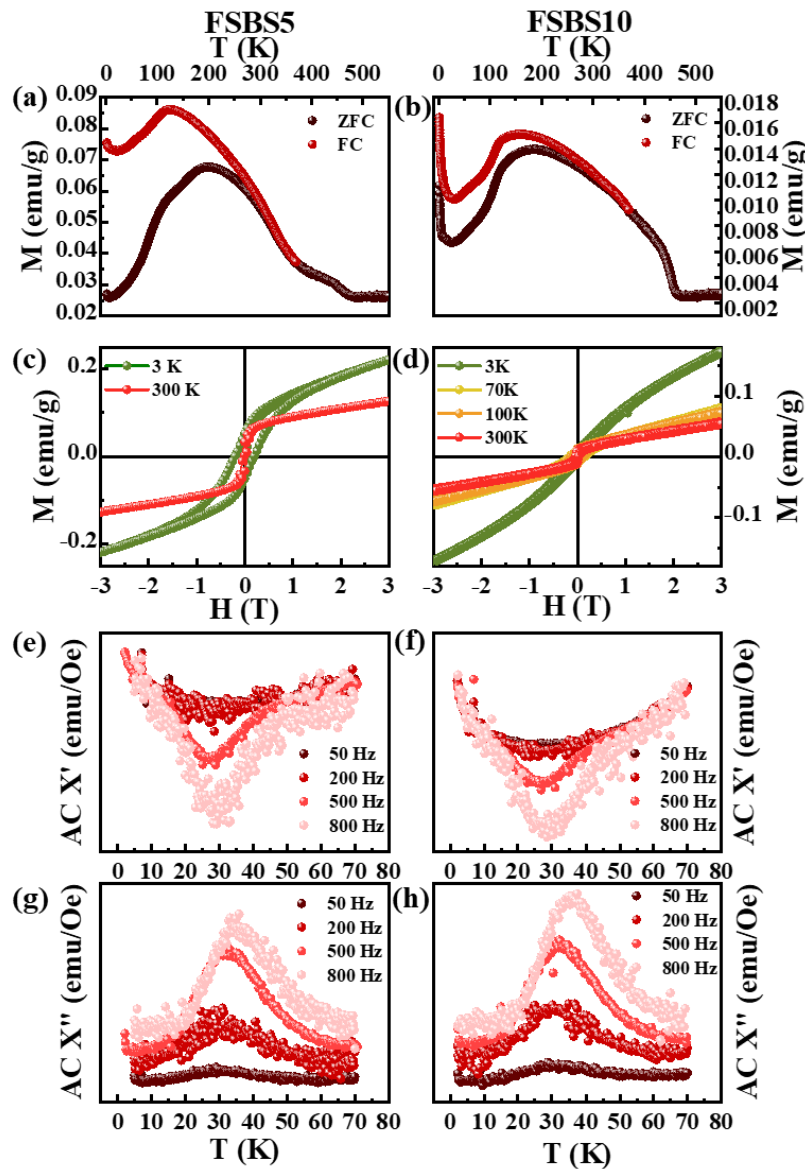
Figure 4.4: (a) and (b) represent the thermal variation of the magnetic moment for FSBS5 and FSBS10, respectively. (c) and (d) exhibits the isothermal moment with varying magnetic fields respectively for FSBS5 and FSBS10. (e, g) and (f, h) demonstrates the real and imaginary part of the ac susceptibility measured at temperature ranging from 2 to 70 K correspondingly for FSBS5 and FSBS10 single crystals.
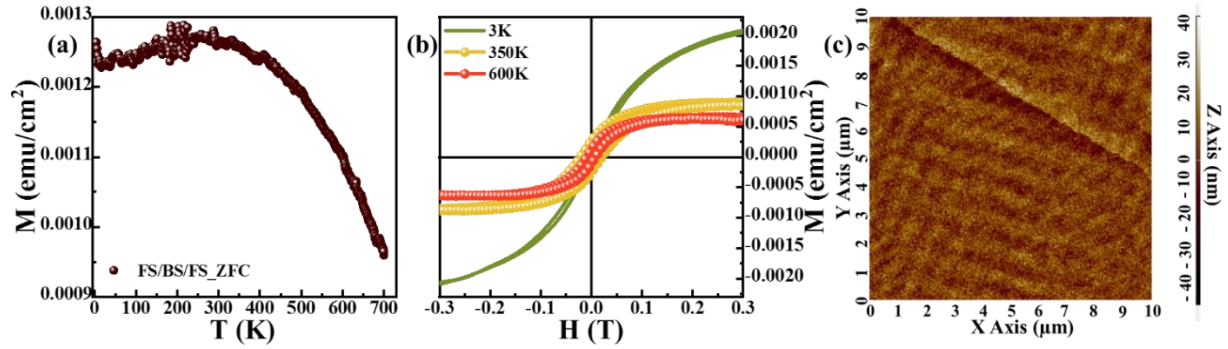
Figure 4.5: (a) Represents the thermal variation of the magnetic moment for FS/BS/FS. (b) Exhibits the isothermal moment with varying magnetic fields corresponding to FS/BS/FS heterostructure. (c) MFM image corresponding to the FS/BS/FS heterostructure is showing a clear magnetic domain structure.

over the FS/BS/FS surface, the room temperature magnetic ordering is vibrant with the anti-parallel orientation of domains as shown in Figure 4.5 (c). Hereby, it can be concluded that the interplay between the magnetic and the spin-orbit coupling associated with topological material at the interfacial proximity introduces the inventive magnetic ordering throughout the surface even at room temperature. However, in the higher temperature, isothermal magnetization curves for (Figure 4.5 (b)) the system shows dominating ferromagnetic ordering, thus showing there is a continuous phase transition from an anti-parallel spin ordering to parallel spin ordering around room temperature. The parallel spin configuration at higher temperatures might be arising due to the presence of iron ions in the FeSe layers which eventually modifies the spin alignment of the Bi_2Se_3 at the interface.

4.2.4 Transport Property

Further to compare the physical properties between the prepared 3-D and 2-D systems we measured longitudinal and transverse resistivity of the systems varying temperature (T) (2 K to 300 K) and magnetic field (-7 T to +7 T), which are demonstrated in Figure 4.6 (a-i) and Figure 4.7 (a-f). The electrical resistivity (ρ) curve (Figure 4.6 (a)) displays the metallic nature of $T^{1.3}$ dependency with temperature for both FSBS5 and FSBS10 single crystals exhibiting the Residual Resistance Ratio (RRR) 4.1 and 5.4

respectively, which are very much similar to the previous results for TIs [40], [42], [143]–[145], [147], [172]. But, when we measure the electrical resistivity for the confined system, it displays striking behavior with varying temperatures from 300 K to 2 K as shown in Figure 4.7 (a). For simplification, we have distinguished the electrical resistivity of the heterostructure in three distinct regions as R-1 (300 K-160 K), R-2 (160 K-50 K), R-3 (<50 K) (Figure 4.7 (a)) to describe the charge carrier evolution and scattering mechanisms throughout the temperature range. Primarily, the resistivity increases with decreasing temperature linearly from 300 K and under 240 K it starts decreasing showing metallic behavior. Such broad semiconducting to metallic transition adjacent to 240 K, which is denoted by R-1 in Figure 4.7 (a) supposed to be related to the plasmon-polaron formation [173]–[175]. However, the increment in resistivity with T^{-1} dependency (as shown in the bottom-right inset of Figure 4.7 (a)) from 300 K to 260 K might be introduced by coulomb drag contributed by plasmon. Actually, the total electrical resistivity as a function of temperature ($\rho(T)$) is the combination of elastic and inelastic interactions. Now, the coulombic interaction among the charge carriers predominantly initiates the elastic scattering, whereas the inelastic scattering is originated merely from the charge carrier interactions like electron-electron (e-e), electron-phonon (e-p), or electron magnon (e-m) scatterings [44], [176]. So, in order to analyze the ascribed changeover, we introduced a relation to associate with the electrical resistivity at higher temperature (R-1) as,

$$\rho(T) = \rho_0 + \rho_2 T^2 + \rho_5 T^5 \qquad (1)$$

Here, ρ_0 symbolizes the residual resistivity, which was evaluated as 17.177 μΩm. The second term corresponding to T^2 represents the delocalized e-e correlation which is an elastic interaction and the T^5-associated term attributed to the e-p interaction mechanism which arises due to the inelastic type scattering. So, from 300 K to 160 K both the e-e and

e-p scattering contribute to the resistivity. But, these two types of interactions generally contribute oppositely depending on the interfacial disorders and variation in temperature. With the careful investigation of the fitting parameters, we found that the e-e contribution is dominating our system in that particular temperature range. Consequently, in the R-2 region from 160 K to 50 K in Figure 4.7 (a), $\rho(T)$ varies with $T^{1/2}$ dependency as,

$$\rho(T) = \rho'_0 + \rho_2 T^{1/2} \tag{2}$$
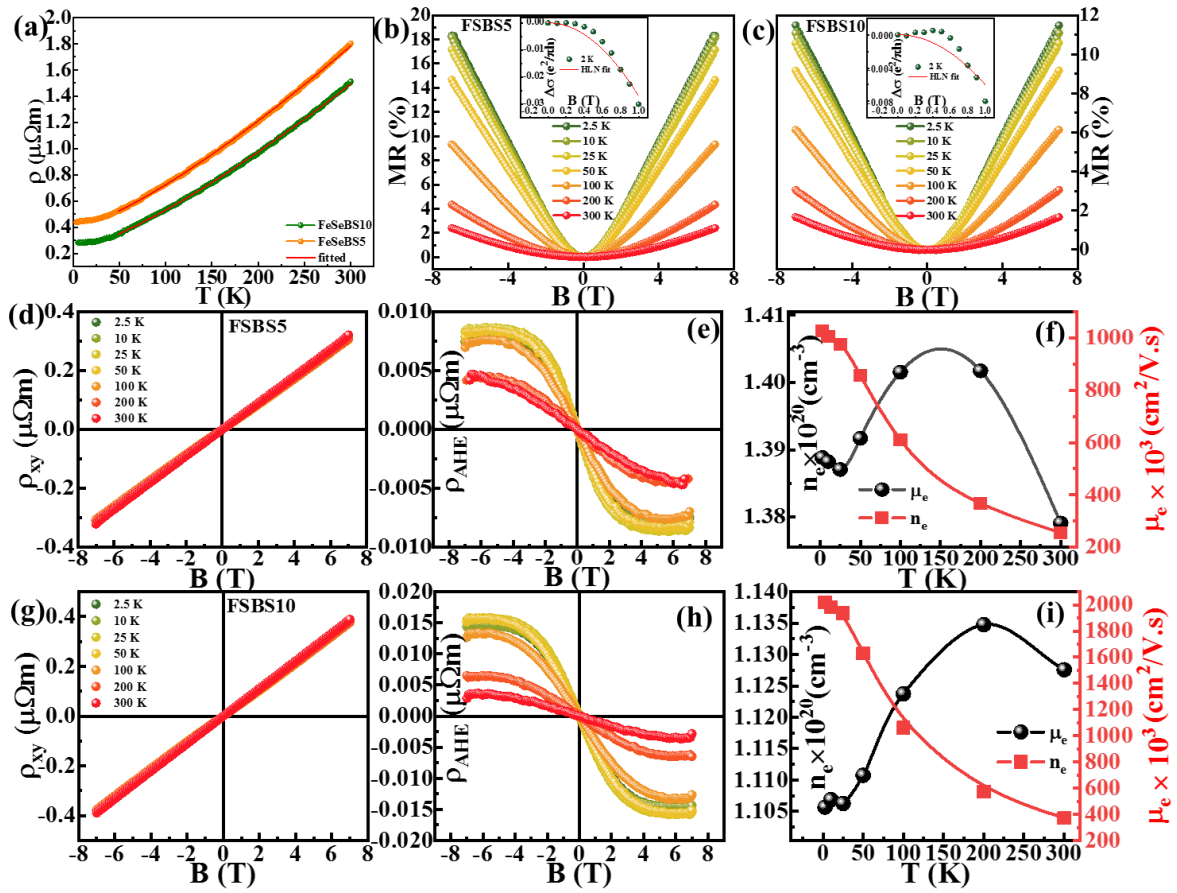
Figure 4.6: (a) Resistivity variation with temperature ranging from 2 to 300 K for FSBS5 and FSBS10 single crystals. Magnetic field dependency of the isothermal magnetoresistance for FSBS5 and FSBS10 are shown in (b) and (c), respectively. We tried to fit the HLN formula in the magnetoconductivity curve below 1 T at 2.5 K for both FSBS5 and FSBS10 as shown correspondingly in the inset of (b) and (c). (d-f) and (g-i) represents the measured hall resistivity with the magnetic field, extracted anomalous hall resistivity with field and the evaluated values of charge density and mobility with temperature for FSBS5 and FSBS10, correspondingly.

Where the residual resistivity ρ'_0 was estimated as 15.35 μΩm and the $T^{1/2}$ term is associated with the e-e correlation arising due to the localization of the carriers at lower temperatures. Further decreasing temperature, resistivity gradually starts raising below 12 K, denoted as R-3 in Figure 4.7 (a). To recognize the possible reason behind such an upturn observed in our 2-D system, an additional term has been assimilated in $\rho(T)$ as,

$$\rho(T) = \rho_{elastic} + \rho_{inelastic} + \rho_{upturn} \tag{3}$$

Focusing on the third term to comprehend the upturn, we tried to fit $\rho(T)$ with *ln T* and $T^{1/2}$ as shown in the inset of Figure 4.7 (b). Apparently, below 12 K *ln T* fitted curve appeared to be a better match with the experimental data points signifying the occurrence of Kondo-like phenomena appearing at low temperatures [44], [177]. Further, the logarithmic increase in electrical resistivity with lowering the temperature was revealed to be exhibiting a characteristic feature of the Kondo effect [41], [178], [179] below 40 K as shown in Figure 4.7 (b), extensively. Herewith, the experimental electrical resistivity data at low temperature was fitted using a simplified Kondo model given by,

$$\rho(T) = \rho''_0 + qT^2 + pT^5 + R_k\left(\frac{T}{T_k}\right) \tag{4}$$

Where ρ''_0 represents the residual resistivity as 16.505 μΩm, and the T^2 and T^5 terms are representing e-e and e-p interactions, respectively as described earlier. Eventually, the last term signifies the spin-modulated Kondo effect, which can be further expressed as an empirical form,

$$R_k\left(\frac{T}{T_k}\right) = R_k(T = 0)\left[\frac{T_k'^2}{T^2 + T_k'^2}\right]^S \tag{5}$$

$$\text{where, } T_k' = \frac{T_k}{\left(2^{1/S} - 1\right)^{1/2}} \tag{6}$$

Here, the value of S was fixed as 0.225. The Kondo temperature (T_k) was evaluated as 6.6 K and the obtained fitting parameters using the Kondo model are listed down in Table 4.2. The obtained parameters recommend a competition between the e-e scattering and the Kondo-associated term. In this context, it is noteworthy that the magnitude of the Kondo-related term R_k is much more superior than the magnitude of q associated with the e-e interaction term, which exhibits the dominance of the Kondo effect in the low-temperature region. The Kondo model incorporates electron scattering in a conducting system in presence of the localized magnetic impurities, which is consistent with the existence of magnetic ordering in the system as described earlier. But we have observed previously that, such Kondo-like property does not exist for our 3-D systems like FSBS5 and FSBS10. This implies that the interlayer proximity strengthens the magnetic ordering in the TI layer enhancing the resistivity at low temperatures. Though the magnetic impurity induces significant magnetic ordering at a large temperature range, it does not reflect in the electrical resistivity property of such a system which needs further observation. Generally, the T^2 dependency of $\rho(T)$ corresponding to e-e scattering for the systems with weak disorders can be described by the classical Fermi liquid (FL) model [180]. But, with cooling down the system, the FL model losses its clarity to describe such Kondo-like abnormality induced in the $\rho(T)$ curve. Such behavior might be explained by quantum correlation and interference taking into account the inelastic interactions and random fluctuations in the electronic states. Further, the RRR was determined as 1.074 for FS/BS/FS which is much less than that of the 3-D bulk systems and the value of resistivity enhances at the order of 100 for the 2-D heterostructure as compared to the single crystals. Such improvement in resistivity value might be a result of the enhanced localization due to the dimensional confinement and the interfacial magnetic pinning effect. Additionally, we evaluated the activation energy of the heterostructure using the relation,
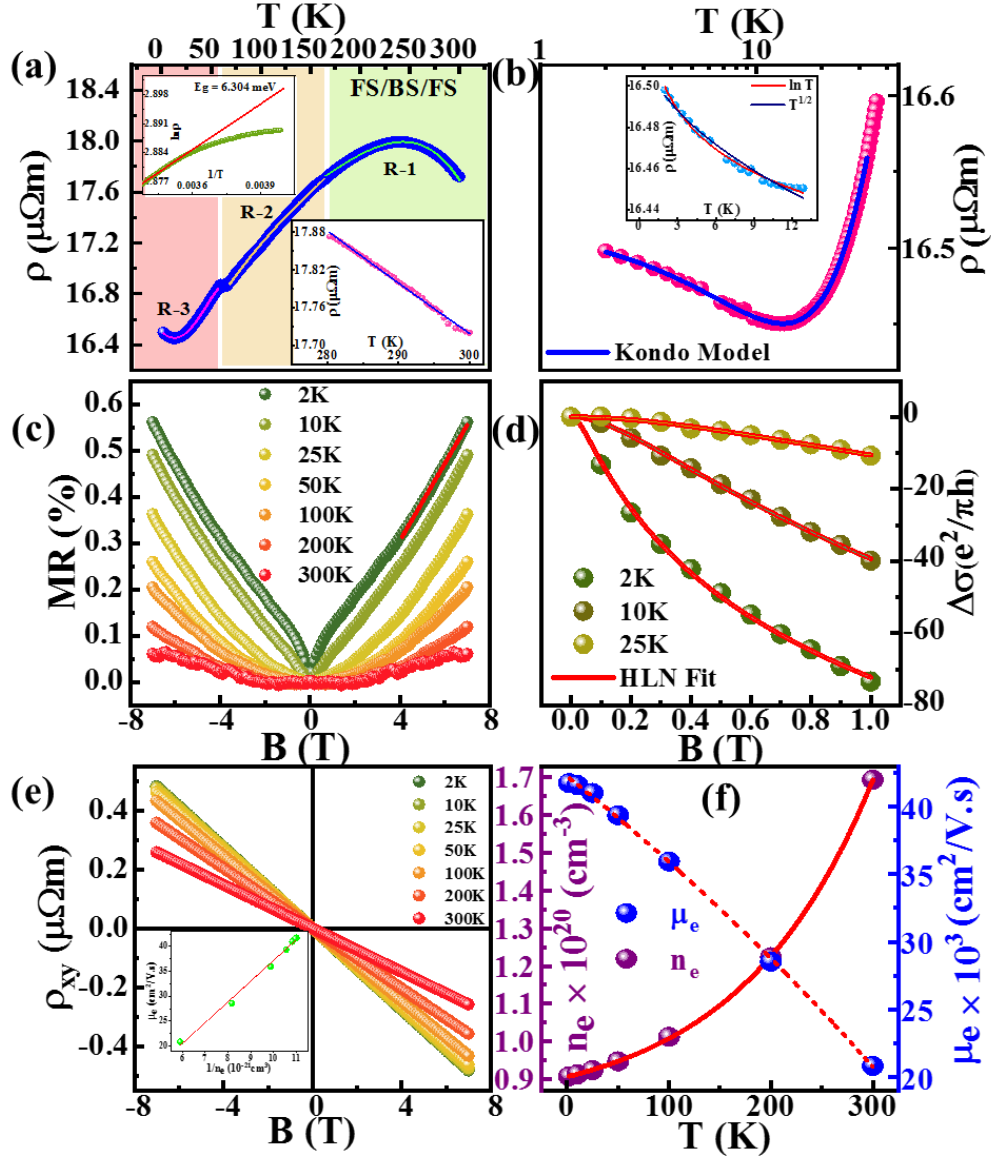
Figure 4.7: (a) Thermal variation of resistivity is exhibited for FS/BS/FS heterostructure. Top-left inset shows the Arrhenius fitted logarithmic value of resistivity. Bottom-right inset shows the linear fitted resistivity data at a temperature range from 280 to 300 K. (b) Kondo model fitted resistance vs temperature in logarithmic scale. Inset represents the ln T and $T^{1/2}$ fitted resistivity data at very low temperatures. (c) MR (%) plotted from -7 T to 7 T at different temperatures ranging from 2 to 300 K. (d) The isothermal magnetoconductivity is fitted with the HLN model below 25 K. (e) The hall resistivity is exhibited from -7 T to 7 T at temperatures ranging from 2 to 300 K. Inset exhibits the mobility variation with charge carrier density. (f) the evaluated values of charge carrier density and mobility are plotted with temperature.

$$\rho = Ae^{\left(\frac{E_g}{2K_BT}\right)} \tag{7}$$

Where E_g exhibits the electrical energy band gap, K_B is the Boltzmann constant. Thus, the

value of E_g was calculated as 6.304 meV for FS/BS/FS from the linearly fitted lnρ vs *1/T*

curve (top-left inset of Figure 4.7 (a)). Usually, in the Kondo model, the logarithmic dependency of $\rho(T)$ incorporates by the spin-modulated transport property of charge carriers. But, irrespective of inducing the magnetic impurity in both 3-D and 2-D systems, only the 2-D system exhibited the Kondo-like upturn. From this observation, we can claim that the conduction electrons at the edge state of the TI layer strongly interact with the localized magnetic impurities in the FM layers and develop the spin-dependent Kondo-like phenomena in the prepared heterostructure. Herewith, the confinement of the electrons increases at the Fermi surface with a gradual decrement of temperature leading to strong spin scattering. The amplitude of such spin scattering has a tendency to extend towards infinity with a further dropping the temperature. This phenomenon is evidenced to be inventing the extensive upturn observed in the low-temperature $\rho(T)$ curve in the present system. There is another possible reason behind the existence of such anomalous behavior of the low-temperature resistivity which is the quantum interference effect [44], [181]. This is a quantum mechanical phenomenon that generally instigates positive magnetoresistance interplaying with the inevitable influence of strong spin-orbit coupling. Such interaction further initiates the changeover from weak anti-localization to weak localization depending on temperature and magnetic field, which we have observed in our present system and described elaborately in the next section. Thus, the interface of the present heterostructure containing entirely different spin textures initiates the Kondo-like upturn in the 2-D system.

Table 4.2 Kondo fitted parameters for the FS/BS/FS system.

Kondo Parameters from RT	FS/BS/FS
ρ_0	16.50577 $\mu\Omega$m
q (e-e interaction)	0.00281 $\mu\Omega$m/K^2
p (e-p interaction)	-7.78428^{-9} $\mu\Omega$m/K^5
R_K	-0.48197 $\mu\Omega$m
T_K (Kondo temperature)	6.61526 K

Magnetoresistance was determined as,

$$MR\% = \left\{ \frac{\rho_{xx}(B) - \rho_{xx}(0)}{\rho_{xx}(0)} \right\} \tag{8}$$

for both the single crystal systems and the heterostructure using the longitudinal resistivity data recorded concerning the magnetic field from -7 T to +7 T [41], [157]. At 2.5 K maximum value of positive linear magnetoresistance (LMR)% was obtained as 18.33 and 11.55 for FSBS5 (Figure 4.6 (b)) and FSBS10 (Figure 4.6 (c)) respectively at ±7 T. Whereas, for FS/BS/FS maximum MR% was determined as 0.56 at 2 K as shown in Figure 4.7 (c). Certainly, with increasing temperature, the suppression of MR% value is observed as a result of enhanced scattering effect and repressed surface state. For the 3-D systems, the MR% exhibits linear behavior at high T as a result of dominating e-p interactions, whereas it deviates to some extent at lower temperatures initiated by spin contribution. The MR% curve for FS/BS/FS displays almost linear dependency on magnetic field (*B*) with a cusp adjacent to 0 T up to 50 K temperature. Whereas, beyond 50 K, the MR% curve attributes parabolic nature. The MR% depends on *B* linearly below 50 K developing a cusp-like behavior which is strongest at the lowest temperature (~ 2.5 K), recommending the existence of a weak anti-localization type quantum interference phenomenon at lower temperatures. But, above 50 K the MR% varies quadratically with the applied magnetic field, signifying the suppression of the WAL effect and enhancement of Weak localization. the consequence of the WAL effect appears to acquire the π-Berry phase suppressing the backscattering of the carriers initiated by the destructive interference among TRS preserved closed paths. Such a stimulating phenomenon augments the classical electronic conductivity quantum mechanically, leading to the WAL effect [43]. For the present heterostructure system, the signature of the WL effect also appears at high temperatures resulting from the constructive interference of the electron waves [182]. The WL is a

quantum effect initiated by the elastic scattering among the charge carriers which is consistent with the electrical resistivity analysis at higher temperatures. Therefore, to comprehend the crossover from WAL to WL and to relate it with the role of topological surface states, we fitted Hikami–Larkin–Nagaoka (HLN) formula on the derived magneto conductivity (MC) data as [38]–[41],

$$\Delta\sigma = \sigma(B) - \sigma(0) = A\left[\psi\left(\frac{1}{2} + \frac{h}{8\pi eBl_\varphi^2}\right) - ln\left(\frac{h}{8\pi eBl_\varphi^2}\right)\right] \tag{9}$$

Where, $A = \frac{\alpha e^2}{\pi h}$ signifies the total number of conduction channels that existed independently in a particular system. The pre-factor value α per conduction channel provides evidence of the strength of SOC in the system. α = 0 for strong magnetic scattering, 0.5 for WAL with strong SOC and 1 for WL with weak SOC [43], [157], [182]–[184]. ψ is the digamma function and l_φ is the phase coherence length. HLN fitted MC statistics below 1T magnetic field at temperatures below 50 K are shown in Figure 4.7 (d). The evaluated values of α and l_φ are listed in Table 4.3 at different temperatures. To determine the conduction per conduction channel, we considered $\Delta\sigma/Z$ in place of $\Delta\sigma$. Where, Z denotes the number of conduction channels as, $Z = t/2nm$. Here, the thickness of the spin-momentum locked system is denoted as t, which was evaluated as ~ 90 nm for the BS layer in FS/BS/FS system described elaborately in the section entitled electronic property. However, one conductance (e^2/h) is contributed by one 2-D layer having 2 quintuple layers (QL) of 2 nm thickness. Herewith, the value of α is ~ 0.47 at 2.5 K which is very close to 0.5 for the present heterostructure. This pre-factor value is evidence of the WAL effect with robust SOC introduced surface state at such a low temperature. At 10 K and 25 K, the HLN formula was fitted well in the MC curve with relatively higher values of α as ~ 0.669 and 0.699, respectively. Thus, the pre-factor value is tending toward 1 with

the enhancement of temperature demonstrating a completion between the WAL and WL effect.

Table 4.3 HLN fitted parameters for the FS/BS/FS heterostructure.

System	T	A	$L\varphi$
FS/BS/FS	2	0.4678	7.7325×10^{-10}
	10	0.6697	3.7099×10^{-10}
	25	0.6993	2.0755×10^{-10}

Also, the dephasing length (~77 nm, 37 nm, 21 nm) reduces consistently with heating up supporting the above-described phenomenon. As a consequence, the MR% displays sharp cusp-like behavior with varying B only when the mean free path (MFT) is less than the dephasing length, which supports our results below 50 K. Nevertheless, the MC curve above 50 K does not follow the HLN formula even at low fields. Henceforth, WAL diminishes at higher temperatures, which is associated with the crossover from WAL to WL for the confined system. Interestingly, a spin-dependent Kondo-like effect exhibiting an infrequent upturn in electrical resistivity was observed at the low-temperature region (<50 K) for the FS/BS/FS heterostructure as shown in Figure 4.7 (b). After analyzing the longitudinal resistivity under the application of magnetic field we are able to accomplish that the TRS-protected enhanced TSS is one of the justifications behind the Kondo effect which is formerly initiated by the spin modulated interfacial proximity effect as described earlier. But, for the single crystals FSBS5 and FSBS10, the MC curves are not converged consistently with the HLN formula event at low field and low-temperature ranges. We have displayed the low field MC curves at 2.5 K for FSBS5 (inset of Figure 4.6 (b)) and FSBS10 (inset of Figure 4.6 (c)) attributing that the HLN formula does not follow the experimental points. Though the single crystalline pure Bi_2Se_3 attributes the WAL effect interplaying

with strong SOC at low T and low B, the iron impurity may cause the suppression of the surface state opening a gap at the Dirac point in the present 3-D system. The quadratic behavior of such MR% curves signify the presence of only weak localization of magnetic domains at the complete range of temperatures. Also, the electrical resistivity displays metallic behavior contributed by dominating e-e elastic scattering as shown in Figure 4.6 (a). As the WAL is consistent with the enhancement of the surface state for the topological insulators, we must notify the development of the unique signature of TSS transport in the confined system as compared to the 3-D systems [185]. This consequence justifies that the interfacial spin-induced 2-D system consumes enhanced gapless surface states over the bulk single crystals improving the applicability of the system as smarter and faster quantum devices. Along with the SOC-facilitated Dirac fermion systems, the WAL phenomenon has immense reportage in various fields [150]. Therefore, the bulk state of TI may demonstrate the WAL effect with quantum correction at low fields similar to the surface state [186]. However, TI bulk state comprises a finite gap which in general leads to the WL effect. Also, the WAL behavior diminishes with the implementation of B for the heterostructure. Therefore, the consistent quantum correction to the bulk state conductivity is given by [42]–[44],

$$\Delta\sigma = -\frac{e^2}{2\pi h}\left[\psi\left(\frac{1}{2}+\frac{B_\Phi}{B}\right) - ln\left(\frac{B_\Phi}{B}\right)\right] + \frac{3\alpha e^2}{2\pi h}\left[\psi\left(\frac{1}{2}+\frac{B\prime_{so}}{B}\right) - ln\left(\frac{B\prime_{so}}{B}\right)\right] \quad (10)$$

The above written QIE formula consists of two contending contributions describing the field-dependent crossover from WAL to WL phenomena. Basically, the first term explains the WAL effect at the lower fields and the rest is accountable for the WL effect at relatively higher magnetic fields [43], [45]. Here,

$$B_\Phi = \frac{h}{8\pi e l_\varphi^2},$$

$$B_{SO} = \frac{h}{8\pi De\tau_{so}},$$

$$B_e = \frac{h}{8\pi De\tau_e},$$

$$\text{And } B'_{SO} = \frac{4}{3}B_{SO} + B_\Phi \tag{11}$$

Here, τ_{so} is the spin-orbit scattering time and τ_e is the elastic scattering time. Hence, τ_φ is considered as electron dephasing time with a relation, $l_\varphi = (D\tau_\varphi)^{1/2}$. Here, D represents the diffusion constant. For the FS/BS/FS heterostructure we tried to fit the isothermal MC data for all the temperatures ranging from 2.5 K to 300 K as shown in Figure 4.8 (a-f). Interestingly, the curve corresponding to the QIE formula deviates from the experimental data at 2.5, 10 and 25 K as displayed in Figure 4.8 (a-c) respectively, whereas it follows the experimental points pretty well at higher temperatures (Figure 4.8 (d-f) for T = 50, 100, 200 K respectively and the inset of Figure 4.8 (f) represents T = 300 K). From the above observation, we can conclude that there does not exist a crossover from the WAL to WL state at lower temperatures. As we have observed earlier, the HLN formula was fitted perfectly below 50 K temperature and 1 T field exhibiting the pre-factor values closer to ~ 0.5, which signifies perfect WAL consequence. Also, we fitted the QIE formula over the MC data below the 1.5 T field in the low T region (R-1) as shown in the inset of Figure 4.8 (c). The fitted curve follows the data points convergingly denoting that only the first term of the QIE formula is effective for the heterostructure at low T. This signifies that, the robust TSS in the 2-D system at temperatures below 50 K dominates over the magnetic spin-induced scattering and the localization of the charge carriers. Also, in this region spin-dependent Kondo effect dominates over e-e and e-p type interactions. This is fascinating that the TSS (WAL) and Kondo-like phenomenon coexist below 50 K, which is conceivable owing to the spin-modulated TI/FM interfacial proximity effect. Whereas,
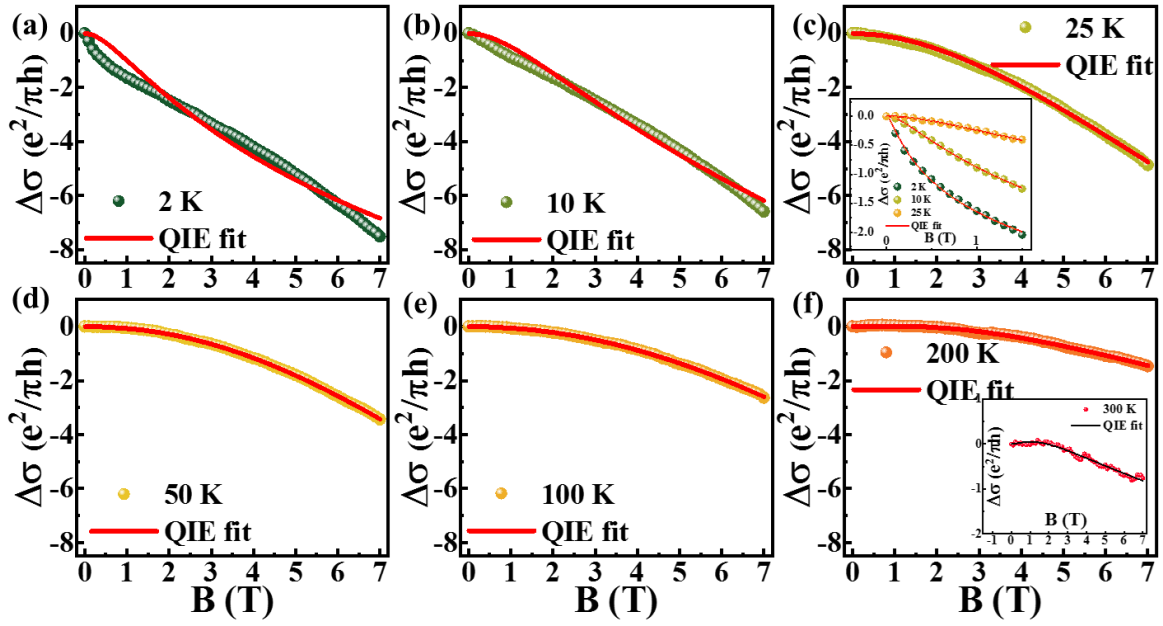
Figure 4.8: The field-dependent isothermal magnetoconductivity is fitted with the QIE model at temperatures 2 K to 200 K respectively in (a) to (f). The inset of (c) represents the QIE fitted resistivity at low temperature and low magnetic field. The QIE model justified with the resistivity at 300 K is shown in the inset of (f).

above 50 K, the changeover occurs smoothly to the WL state. Above, 50 K the WL effect is dominating, as the pre-factor value was evaluated to be greater than unity and the spin-orbit dephasing length is relatively higher. Also, in this temperature region, the localized e-e scattering is dominating in accordance with the electrical resistivity analysis, which is consistent with the present results.

Further, transverse resistivity which is commonly known as hall resistivity (ρ_{xy}) was measured as a function of the magnetic field at different temperatures in order to estimate the mobility and carrier concentration for both the single crystals and the heterostructure. For FSBS5 and FSBS10 bulk single crystals, the variation of hall resistivity as a function of the magnetic field at different temperatures are shown in Figure 4.6 (d) and Figure 4.6 (g) respectively. The exhibited positive slope of hall resistivity indicates that the dominating charge carriers are holes (p-type), while for pure Bi_2Se_3 the charge carriers are reported as electrons (n-type) [40], [42]. Thus, the carrier change-over from the n-type to

the p-type might be caused by the presence of Fe ions, which may create the antisite disorder in our system [143]. Also, the ρ_{xy} exhibits certain anomalies with the applied field for both single crystals. We extracted the anomalous hall contribution (ρ_{AHE}) [146], [147] from the total ρ_{xy} data and plotted it with the field at different temperatures as shown in Figure 4.6 (e) and Figure 4.6 (h), respectively. Such anomaly possibly is initiated by the screw (asymmetric) scattering, side jump, or intrinsic contribution in the crystals. For the present systems, magnetic impurity persuaded spin arrangement might be the primary reason behind such anomaly in transverse resistivity as the magnetic ordering is present at a wide range of temperatures. Further, the estimated values of carrier concentration (n_e) and carrier mobility (μ_e) are plotted with temperature as shown in Figure 4.6 (f) and Figure 4.6 (i), respectively for the 5% and 10% systems. Furthermore, the carrier concentration mostly increases with temperature suggesting the dominance of bulk contribution with temperature [187]. But, the Bi_2Se_3 associated heterostructure shows linear behavior of ρ_{xy} with a negative slope (Figure 4.7 (e)), suggesting that the major transport carriers are electrons that behave completely differently from the bulk crystals. The evaluated value of carrier concentration and carrier mobility from hall data at different temperatures are also shown in the insets of Figure 4.7(a, b). Interestingly, the value of mobility decreases significantly for the heterostructure as compared to the bulk systems possibly due to the dimensional confinement-assisted localization of charge carriers in the 2-D system. Also, it is noteworthy that the confined system does not possess anomalous hall contribution, nonetheless existing with interfacial magnetic domains as designated earlier. Thus, in our system, the anomalous hall effect appears only for the magnetic impurity-induced bulk single crystals. Therefore, the Kondo effect is strongly anticipated as a consequence of the spin induced interfacial proximity of the FS/BS/FS heterostructure. Kondo-like fascinating phenomenon coexisting with weak anti localization at very low temperature exhibiting

enormous edge state improves the applicability of such spin-modulated 2-D confined system in the field of forthcoming faster computation.

4.3 Conclusions and Prospects

We prepared FSBS5 and FSBS10 single crystals using the modified Bridgeman method and afterward prepared FS/BS/FS layered structures by using PLD to compare the structural, electronic, physical and magnetic properties between the bulk and the confined systems. After confirming the structural and morphological transparency of both the systems, the XPS spectra were analyzed in depth comparing all the present elements Bi, Se, and Fe in both the bulk and low dimensional systems. From the depth profile analysis of the heterostructure, we succeed to draw a clear matrix of the layers and interfaces along the cross-sectional plane. Further, the physical and magnetic properties were investigated to enlighten the effect of strain-induced dimensional confinement on the 2-D system. Remarkably, the positive magnetic moment sustained beyond 300 K for both 3-D and 2-D systems. Though the single crystalline FSBS5 and FSBS10 exhibited distinct magnetic transitions below 500 K, the spin-induced topological thin film shows magnetic properties over all temperature ranges, which is very much favourable for spintronic applications. Further, the resistivity curve for the single crystals exhibited metallic nature whereas it was eccentrically modified for the FS/BS/FS heterostructure demonstrating a semiconducting to metallic transition near 240 K and exhibiting Kondo-like nature below 12 K. Such uncharacteristic behavior in resistivity at certainly low temperature justifies the manifestation of interfacial magnetic domain structures. This is also consistent with the dominating antiferromagnetic ordering in the FS/BS/FS heterostructure displayed at 3 K. In addition, The WAL effect is dominating in the heterostructure at lower temperatures admitting the augmentation of the surface state at lower dimensions. But, the single crystalline FSBS5 and FSBS10 are exhibiting positive LMR with WL and AHE at

temperature ranges from 2 K to 300 K. Whereas, the confined system comprehends the localization of well-organized spins at the interfaces, which reduces the mobility of the heterostructure as compared to the bulk crystals by the order of 100 and the perpendicular resistivity does not exhibit any anomaly for this system. Thus, irrespective of the fact that the interfacial magnetic impurity adequately causes disruption in TRS emerging a finite gap at the Dirac point, the detention in dimensionality effectively enhances the surface state in such a 2-D layered system. The interfacial magnetic domains in the confined systems are exhibiting strong electronic and magnetic properties modifying the surface states of the system providing us with a wide range of temperatures to apply directly as memory and spintronic devices.